J|A|C|S
JOURNAL OF THE AMERICAN CHEMICAL SOCIETY

ARTICLE

pubs.acs.org/JACS

Highly Stable Cooperative Distortion in a Weak Jahn−Teller d^2 Cation: Perovskite-Type $ScVO_3$ Obtained by High-Pressure and High-Temperature Transformation from Bixbyite

Elizabeth Castillo-Martínez,[*,†,∥] Mario Bieringer,[*,‡] Shahid P. Shafi,[‡] Lachlan M.D. Cranswick,[§,⊥] and Miguel Ángel Alario-Franco[†]

[†]Departamento de Química Inorgánica & Laboratorio Complutense de Altas Presiones, Facultad de Ciencias Químicas, Universidad Complutense de Madrid, 28040 Madrid, Spain

[‡]Department of Chemistry, University of Manitoba, Winnipeg, Manitoba, R3T 2N2, Canada

[§]Canadian Neutron Beam Centre, National Research Council Canada, Chalk River Laboratories, Chalk River, Ontario, K0J 1J0, Canada

Supporting Information

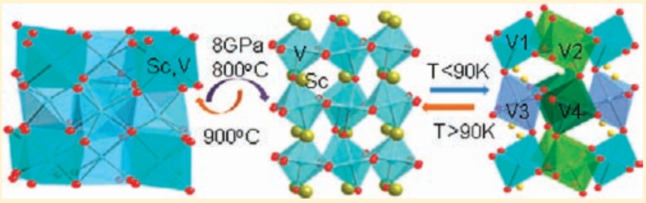

ABSTRACT: A novel $ScVO_3$ perovskite phase has been synthesized at 8 GPa and 1073 K from the cation-disordered bixbyite-type $ScVO_3$. The new perovskite has orthorhombic symmetry at room temperature, space group *Pnma*, and lattice parameters $a = 5.4006(2)$ Å, $b = 7.5011(2)$ Å, and $c = 5.0706(1)$ Å with Sc^{3+} and V^{3+} ions fully ordered on the A and B sites of the perovskite cell. The vanadium oxygen octahedra $[V-O_6]$ display cooperative Jahn−Teller (JT) type distortions, with predominance of the tetragonal Q_3 over the orthorhombic Q_2 JT modes. The orthorhombic perovskite shows Arrhenius-type electrical conductivity and undergoes a transition to triclinic symmetry space group *P*-1 close to 90 K. Below 60 K, the magnetic moments of the 4 nonequivalent vanadium ions undergo magnetic long-range ordering, resulting in a magnetic superstructure of the perovskite cell with propagation vector (0.5, 0, 0.5). The magnetic moments are confined to the *xz* plane and establish a close to zigzag antiferromagnetic mode.

1. INTRODUCTION

Perovskites are very frequently encountered in materials science and geology. For many applications it is possible to think of a material with the perovskite structure of stoichiometry ABX_3 or a closely related superstructure of this chemical *chameleon*: from ferroelectrics and piezoelectrics to giant magnetorresitant phases,[1] superconducting compounds,[2] or materials for fuel cells[3] and catalytic exhausts.[4] At the same time, this structure type and its temperature- and pressure-driven transitions have important implications for the behavior and understanding of the earth mantle.[5]

The versatility of the perovskite structure, with general formula ABX_3, is based on the ability of the AX_3 packing to accommodate a large variety of A and B cations with different A−X and B−X distances. For simple oxide perovskites ABO_3, the symmetry of the resultant compound can somehow be anticipated through the geometrical relationship between both cation−anion distances.[6] In this way, if the Goldschmidt tolerance factor t, $t = (r_A + r_o)/(\sqrt{2}(r_B + r_o))$, is 1 (where r_A, r_B, and r_o are the ionic radii of A, B, and the oxygen, respectively), a highly symmetric cubic perovskite is formed in which B is in the center of a regular octahedron and A in the center of a perfect cuboctahedron. For $t > 1$ equilibrium is reached through face sharing of BO_6 octahedra (and sometimes small concentrations of anion vacancies), yielding hexagonal perovskites. Above a critical value t_c, for a certain range of t, $t_c < t < 1$ cooperative rotations of the octahedra along the one, two, or three axis of the cubic parent yield lower symmetry perovskites.[7,8] Below t_c however other structural types are observed. Transitions based on the appearance, disappearance, and change of the cooperative octahedral tilting have been observed in many perovskite systems upon heating or cooling,[9] substitution of the different cations,[10] and application of high pressure.[11]

High pressure itself has been used in many instances to induce phase transitions and can also provide access to metastable ambient pressure phases including perovskite-related structures. For example, it has been shown that high pressure induces reversible charge transfer with melting of charge ordering in $BiNiO_3$,[12] and irreversible phase transformations from ilmenite-type phases into metastable perovskites have been observed.[13]

Related examples of the use of high pressures in stabilizing many perovskite polytypes are the charge density wave system $BaIrO_3$[14] and several members of the family of ferromagnetic superconductors Ru-1212.[15] Of special relevance to the present work is the possibility of inducing "cationic ordering" in binary oxides A_2O_3, as, for example, in the transformation from corundum-type

Received: October 28, 2010
Published: May 16, 2011

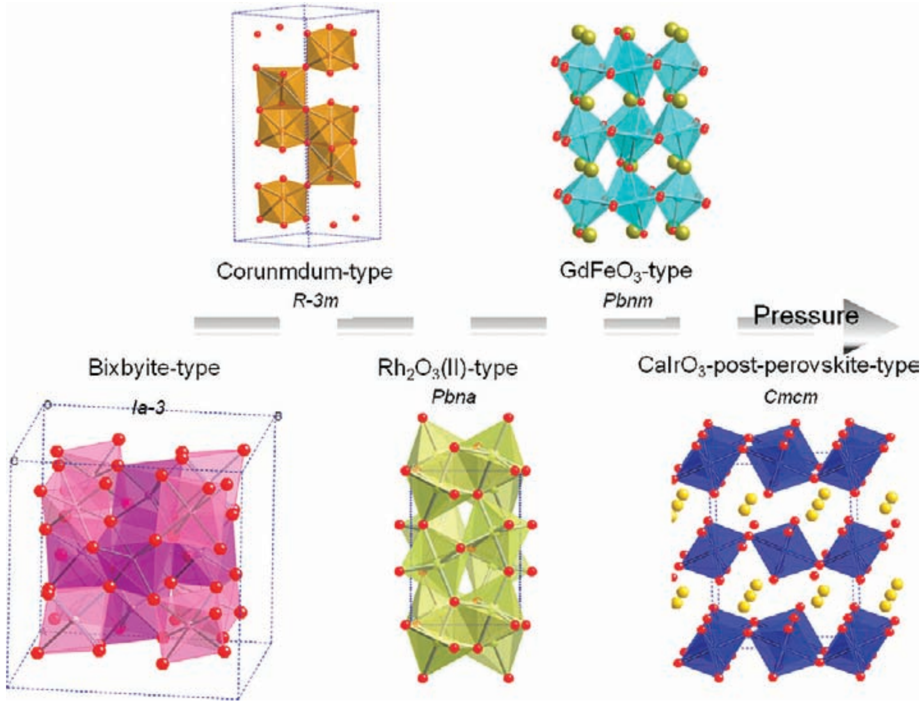

Figure 1. Phase transformations in AA′O$_3$ structure types under high pressure.

structure of Al_2O_3 to Rh_2O_3-(II),[16] and, further, to the postperovskite (the so-called $CaIrO_3$ type at higher pressures[17] or from the bixbyite-type Fe_2O_3 that, successively, transforms into the Rh_2O_3(II),[18] the orthorhombic perovskite ($GdFeO_3$-type),[19] and finally to the postperovskite ($CaIrO_3$-type)[20] at 55, 65, and 96 GPa, respectively. These and other examples account for the trend of structural transitions with pressure shown in Figure 1 with A and A′ randomly occupying the same crystallographic sites in the bixbyite, corundum, and Rh_2O_3(II) types but distinct crystallographic sites in the perovskite and postperovskite types and suggests that any transition along the direction of the arrow could, eventually, be realized if the appropriate thermodynamic conditions of pressure, temperature, and time are used.

$ScVO_3$, the object of the present work, crystallizes at ambient pressure in the cubic bixbyite structure (space group $Ia\overline{3}$) with Sc^{3+} and V^{3+} statistically disordered on the 8b and 24d sites.[21] In contrast, AVO_3 systems with A cations larger than In^{3+} such as Lu^{3+}, other rare earths,[22,23] Y^{3+},[24] and even the solid solution $Sc_{(1-x)}Lu_xVO_3$ with $x \geq 0.58$[25] crystallize in the fully ordered perovskite structure with R^{3+} (R = rare earth, Y and Sc) located in the A site and V^{3+} occupying the B site. Scandium along with yttrium is frequently regarded as rare earths, and therefore, YVO_3 is usually included in systematic studies of RVO_3. $ScVO_3$, not having been obtained as a perovskite until now, is so far the smallest ionic radius R member of the RVO_3 and extends the range of existence and possible phenomena observed in that perovskite family. Notably, other orthorhombic perovskites with such small A cations such as $ScCrO_3$ and $InCrO_3$ have been formed at 45 kbar, 1200 °C and 65 kbar, 1250 °C, respectively.[26,27]

One of the most relevant aspects of the orthovanadates, RVO_3, is the stabilization of a JT distortion at low temperatures and the coupling of this structural distortion with the magnetic ordering of the spins of the vanadium sublattice which at low temperature can result in magnetization reversals due to competing magnetic interactions.[28] The octahedrally coordinated d^2 ion, V^{3+}, is a weak Jahn−Teller ion that may undergo cooperative Jahn−Teller distortions that split the degeneracy of the t_{2g} states.[29] For V^{3+} perovskites orbital ordering has only been observed at low temperatures,[30] whereas strong JT cations, such as the d^4 ion Mn^{3+} in $LaMnO_3$, show cooperative distortions well above room temperature.[31] The cooperative JT distortion is manifested as orbital ordering with preferential filling of the t_{2g} orbitals, the most common JT mode being orthorhombic Q_2, with a pattern of medium M−O distances along the $2a_p{\sim}b$ axis (in *Pnma* setting) or *c* axis (in *Pbnm* setting) of an orthorhombic perovskite and short and long M−O distances alternating in the $\sqrt{2}a_p \times \sqrt{2}a_p$ plane where a_p is the basic cubic perovskite subcell parameter. Another type of JT distortion is the tetragonal Q_3 mode that leads to elongated octahedra, but it has rarely been reported for simple oxide perovskites.[32]

The more commonly observed JT distortion, Q_2, coupled to the octahedral tilting is responsible for various crystallographic and magnetic transitions occurring at low temperatures which have been extensively studied.[30,33] Depending on the interplay between octahedral tilting and Jahn−Teller distortion different symmetries and associated with them different magnetic structures have been observed.[34,35] For RVO_3 with large R cations, a transition from orthorhombic to monoclinic symmetry concomitant with C-type orbital ordering occurs at low temperatures.[36] However, for smaller R ions with larger octahedral tilting G-type orbital ordering without a change in symmetry stabilizes at temperatures between 160 and 200 K, and this induces a C-type antiferromagnetic spin ordering at lower temperatures (the temperature decreases for the smaller R). A second crystallographic and magnetic transition to C-type orbital ordering and G-type spin ordering takes place at even lower temperatures, with the temperature for the second orbital ordering (T_{oo2}) increases for smaller R ions.[37]

It is the aim of this work to present the results concerning the synthesis of a novel $ScVO_3$ perovskite by means of high-temperature and high-pressure phase transformations from the cation disorderd bixbyite. This perovskite can be transformed back into the original bixbyite by annealing at ambient pressure. We also discuss its crystal structure, including the octahedral tilting, and emphasize the Jahn–Teller-type distortion and the resulting orbital ordering. In addition low-temperature crystallographic and magnetic transitions are described. Finally, we correlate the structural, magnetic, and transport properties of the $ScVO_3$ perovskite with those observed in other members of the RVO_3 family highlighting the new findings.

2. EXPERIMENTAL SECTION

$ScVO_3$ bixbyite was synthesized in a two-step method. In the first step $ScVO_4$ was prepared from Sc_2O_3 (Alfa Aesar 99.99%) and NH_4VO_3 (Cerac 99.9%) at 1100 °C in air. In the second step pure bixbyite $ScVO_3$ is obtained by reduction of zircon-type $ScVO_4$ with H_2 at 1100 °C.[38] The high-pressure transformation from the bixbyite to the perovskite-type $ScVO_3$ was performed in a Belt-type apparatus.[39] The bixbyite powder was pressed into 3 mm diameter gold capsules. Samples were first pressurized to its target pressure at a constant rate, and after 5 min of pressure stabilization they were heated to the target temperature and annealed for 30 min. The temperature was quenched before slowly releasing the pressure.

As-synthesized powder samples were studied by conventional powder X-ray diffraction on an X'Pert PRO ALPHA 1 (Panalytical) instrument with a germanium monochromator (Cu $K\alpha_1$ = 1.540598 Å). XRD data for structure refinement were collected for 12 h in the 2θ X-ray range from 2° to 90° with a step size of 0.0167°.

In-situ powder X-ray diffraction experiments were carried out on a PANalytical X'Pert Pro diffractometer, with an Anton Paar HTK2000 high-temperature chamber equipped with a platinum strip heater. Diffractograms were obtained in the 2θ range from 2° to 90° with a step size of 0.0167°. The powdered $ScVO_3$ perovskite sample was mounted as a thin layer and heated in a 1:3 CO:He gas flow. Diffraction patterns were measured for 20 min (300 min for Rietveld refinement) from 25 to 1000 °C at 25 °C increments. The temperature of the furnace is accurate within at least 5 °C between room temperature and 1200 °C.

Neutron powder diffraction (NPD) data were first collected on the medium-resolution 800 wire powder neutron diffractometer C2 operated by the National Research Council Canada at Chalk River at room temperature. Low-temperature neutron diffractograms were collected using a Janis closed cycle refrigerator. Diffractograms were measured between 3.1 K and room temperature with neutron wavelengths λ = 2.3698(4) Å ($5° \leq 2\theta \leq 85°$) and λ = 1.3300(2) Å ($35° \leq \theta \leq 115°$) and default detector wire spacing of 0.1002° steps. Note that a 100 mg sample with 6% starting material impurity was used for these neutron diffraction experiments.

Low-temperature powder neutron diffraction experiments were carried out on a 58 mg phase pure sample in a cylindrical (4 mm diameter) vanadium sample can on the high-flux diffractometer D20 at the ILL in Grenoble, France. For the high-flux (HF) diffraction experiments a wavelength of λ = 2.41 Å with maximized neutron flux and a takeoff angle of $2\theta_T$ = 42° and using a pyrolytic graphite monochromator was selected in order to follow magnetic scattering between 2 and 60 K. High-resolution (HR) neutron diffraction data were collected between 2 and 296 K with a neutron wavelength of λ = 1.87 Å (take-off angle $2\theta_T$ = 118°) using a Ge(115) monochromator. In order to reduce the incoherent scattering from the vanadium shielding of the cryostat, cadmium was used to wrap part of the empty can and diffraction peaks corresponding to cadmium also appear in the patterns.

Crystal and magnetic structures were Rietveld refined using the JANA[40] and Fullprof programs.[41] Room-temperature lattice parameters from the refinement of XRD data were used to refine the high-resolution neutron wavelength (λ = 1.87 Å), and the 2 K data set refined from this wavelength was used to refine the λ = 2.41 Å. The background was modeled as a cubic spline function. The peak shapes were modeled with pseudo-Voigt functions. Scale factors, zero point, unit cell constants, Sc and O atomic positions, and temperature factors as well as Sc site occupancies were refined simultaneously. Temperature factors were constrained to be equal for all oxygen atoms and equal for all scandium atoms.

For transmission electron microscopy (TEM) studies powdered samples were ground with *n*-butyl alcohol, and a drop of the suspension was collected on a holey carbon-coated copper grid. Selected area electron diffraction (SAED) was performed with a JEOL JEM FX2000 microscope equipped with a double tilt ±45° sample holder, working at 200 keV. HRTEM was carried out on a JEOL JEM 3000FEG microscope, with C_S = 0.6 nm, operating at 300 keV. The composition of the perovskite crystals was analyzed in the TEM by X-ray energy-dispersive spectroscopy with a Link Pentafet 5947 model using bixbyite $ScVO_3$ as standard for *k* factor calibration.

Magnetic susceptibility measurements were performed over the temperature range 2–300 K using a SQUID Quantum Design XL-MPMS magnetometer under zero-field-cooling (ZFC) and field-cooling (FC) conditions employing a constant external magnetic field of 1000 and 10000 Oe (1 T). Magnetization vs applied magnetic field was recorded at constant temperatures in the ZFC mode. When the desired temperature is reached, the magnetic field is raised up to 5 T in the SQUID (or 9 T in the PPMS), decreased down to −5 T (−9 T), and finally increased again to 5 T(9 T) in order to close the cycle.

Resistance and specific heat measurements were carried out in the temperature range 2–300 K using a Quantum Design PPMS at zero field and at an applied magnetic field of 9 T. Resistance measurements were performed on as-synthesized sintered disks with the four-probe method. Silver paste was used to get good electrical contact between the copper wires and the bulk sample. For the heat capacity measurements an addendum of the puck with low-temperature grease (for good thermal contact) was measured and subtracted from the total data of the sample.

3. RESULTS

The $ScVO_3$ bixbyite starting material is a brownish-black powder. The evolution of the transformation from bixbyite to perovskite in $ScVO_3$ was followed by ex-situ XRD of the quenched powders at ambient pressure and room temperature after opening the gold capsule used for high-pressure and high-temperature treatment. Figure 2A shows that the conversion is not complete at pressures up to 6 GPa and temperatures of 1000 °C. A single phase is obtained at 8 GPa and 800 °C; the resulting black powder shows a shinier luster than the starting material.

3.1. Crystal Structure Determination of the Novel Perovskite $ScVO_3$. *3.1.1. Room-Temperature X-ray and Neutron Diffraction Data.* The PXRD pattern collected at room temperature corresponds to that of an orthorhombic perovskite. Rietveld refinement of the PXRD data was performed in order to confirm the symmetry and to determine the lattice parameters and starting atomic positions. A good fit was obtained for space group no.

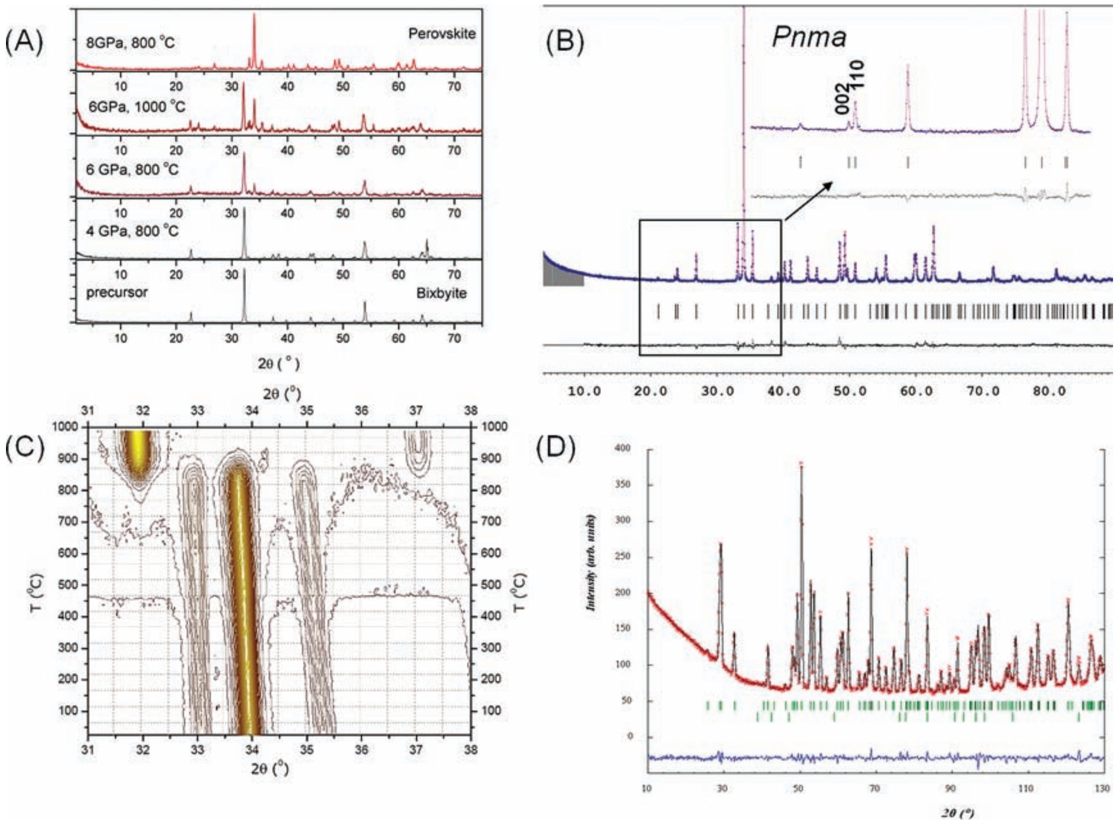

Figure 2. (A) PXRD patterns of the reaction products after treating the precursor bixbyite at different high-pressure high-temperature conditions. (B) Rietveld refinement of the PXRD data of $ScVO_3$; the inset shows details of the region of the (002) and (110) reflections. (C) Powder X-ray diffraction contour plots of in-situ high-temperature annealing of $ScVO_3$ (perovskite) in 1:3 CO:He flow showing the conversion to its native bixbyite phase. (D) Rietveld refinement of the neutron diffraction profile collected at 296 K on the powder diffractometer D20 using a wavelength $\lambda = 1.87$ Å. Red is the observed intensity, black is the calculated intensity, and blue is the difference. Top markers are $ScVO_3$, and bottom markers are due to the Cd shielding.

62 *Pnma* (reliability factors $R_p = 5.56$, $R_{wp} = 7.71$, and $R_B = 6.82$, $\chi^2 = 2.05$). Figure 2B shows the Rietveld fit of the PXRD pattern from $2\theta = 10°$ to $90°$; the insert emphasizes the low-angle region of the Rietveld plot. Figure 2D shows the Rietveld plot for high-resolution neutron data collected at room temperature.

The Rietveld refinement of the powder neutron diffraction data collected at room temperature confirms that the A position is only occupied by Sc and that the B site is only occupied by V. When exchanging the Sc and V positions a very poor fit is obtained. There is however a slight deficiency of less than 5% on the scandium position.

The negative isotropic thermal displacement parameters obtained with the refinement of the XRD data become positive in the refinement of the neutron data. It is expected that neutron diffraction data with its excellent sensitivity for oxygen positions and occupancies gives a more reliable structure than X-ray diffraction. Atomic positions and interatomic distances are listed in Tables 1 and 2, respectively. The tilting angle about the [111] direction, $\varphi_{(111)}$, the angle with respect to the basal plane, ω, the degree of orthorhombic distortion, s, and the octahedral distortion parameter, Δ, have also been calculated and are listed in Table 2.

3.1.2. Microstructure: Electron Microscopy. The cationic composition, determined on several crystallites by EDX analysis in the transmission electron microscope, is the expected one: 50(1) % Sc, 50(1) % V. Selected area electron diffraction (SAED) observations confirm the existence of an orthorhombic cell with metric $\sim(2a_p)^{1/2} \times 2a_p \times (2a_p)^{1/2}$. Figure 3A shows the [010] zone axis pattern indexed on the basis of this orthorhombic cell (space group 62, *Pnma* setting). The weaker (h00) reflections with h odd (which are not allowed in space group *Pnma*) appear as a result of a double-diffraction phenomena, and accordingly, they do not appear in the [001] zone axis (Figure 3B).

The double-perovskite parameter, $2\mathbf{a}_p$ is demonstrated by the extra spot at one-half of $\mathbf{b}_p^*$ in both the [001] and the [−101] zone axes patterns (Figure 3B and 3C). The high-resolution transmission electron microscope (HRTEM) image along [−101] (Figure 3D) shows rows of bright contrast separated by 7.6 Å, as pointed out by arrows, which correspond to the $\mathbf{b}_o \sim 2\mathbf{a}_p$ axis.

Structural microdomains, frequently found in orthorhombic perovskites, are observed by neither electron diffraction nor imaging. At room temperature the V−O−V angles in $ScVO_3$ are 137.9(3)° and 133.7(4)° (Table 2) yielding an octahedral tilting angle of $\varphi_{111} = 26°$, which is larger than the threshold angle for multi-twinning to appear $\varphi_{111} = 17.2°$;[42] this also explains the lack of domains in the electron diffraction patterns. However, some planar defects along $\mathbf{b}_o$ are seen, as the one appearing in the HRTEM image indicated by the long black arrow; these are responsible for the streaking along $\mathbf{b}^*$ in the electron diffraction pattern, indicated by a black arrow in Figure 3C.

3.1.3. Thermal Stability of the $ScVO_3$ Perovskite Phase: High-Temperature X-ray Diffraction. The thermal evolution of the

Table 1. Refined Lattice and Structural Parameters for Perovskite ScVO$_3$ at All Temperatures[a]

	Pnma				*P*-1			
ScVO$_3$	296 K	150 K	120 K		90 K	60 K	30 K	2 K
a (Å)	5.4014(2)	5.4009(2)	5.4009(2)	*a* (Å)	5.40020 (12)	5.39824 (14)	5.3975 (2)	5.3976 (2)
b (Å)	7.4939(2)	7.4899(2)	7.4892(2)	*b* (Å)	7.4917 (2)	7.4955 (2)	7.4956 (3)	7.4968 (3)
c (Å)	5.0745(2)	5.0646(2)	5.0629(2)	*c* (Å)	5.06186 (15)	5.06151 (17)	5.0610 (2)	5.0609 (2)
				α	90.269 (3)	90.420 (3)	90.442 (3)	90.446 (3)
				β	90.0	90.229 (4)	90.180 (5)	90.150 (6)
				γ	90.0	89.975 (4)	89.975 (5)	89.982 (6)
vol. (Å^3)	205.4 (5)	204.88 (1)	204.78 (1)	vol. (Å^3)	204.78 (1)	204.79 (1)	204.75 (2)	204.78 (1)
Sc *x*	0.0688 (3)	0. 0698 (3)	0.0699 (4)	Sc1 *x*	0.071 (2)	0.0690 (8)	0.0694 (11)	0.0690 (12)
				Sc1 *y*	0.2502 (13)	0.2529 (9)	0.2538 (11)	0.2546 (12)
Sc *z*	0.978 (3)	0.9763 (4)	0.9756 (4)	Sc1 *z*	0.9823 (17)	0.9786 (9)	0.9750 (11)	0.9747 (13)
				Occ	0.481 (10)	0.486 (6)	0.48 (8)	0.496 (8)
				Sc2 *x*	0.570 (3)	0.5723 (9)	0.5729 (12)	0.5737 (13)
				Sc2 *y*	0.2443 (13)	0.2439 (10)	0.2441 (12)	0.2452 (14)
				Sc2 *z*	−0.4698 (18)	−0.4727 (10)	−0.4767 (13)	−0.4759 (15)
Occ	0.456 (5)	0.463 (5)	0.461 (6)	*Occ*	0.443 (9)	0.439 (6)	0.443 (8)	0.438 (8)
B_{iso}	0.68 (4)	0.47 (5)	0.45 (5)	B_{iso}	0.45 (4)	0.50 (5)	0.62 (5)	0.54 (5)
V B_{iso}	4,35 (13)	0.4 (9)	−0.4 (9)	V 1,2,3,4 B_{iso}	0.646	0.646	0.646	0.646
O1 *x*	0.4348 (6)	0.4349 (7)	0.4347 (7)	O1 *x*	0.443 (7)	0.4333 (13)	0.4332 (16)	0.4326 (18)
				O1 *y*	0.243 (2)	0.2462 (18)	0.247 (2)	0.245 (2)
O1 *z*	0.1419 (5)	0.1417 (6)	0.1415 (6)	O1 *z*	0.138 (4)	0.1367 (18)	0.141 (2)	0.142 (3)
B_{iso}	0.80 (9)	0.48 (10)	0.49 (11)					
				O2 *x*	0.928 (6)	0.9340 (12)	0.9363 (16)	0.9376 (18)
				O2 *y*	0.249 (3)	0.2519 (18)	0.251 (2)	0.252 (2)
				O2 *z*	0.357 (4)	0.3512 (18)	0.351 (2)	0.354 (3)
O2 *x*	0.3128 (5)	0.3133 (5)	0.3134 (6)	O3 *x*	0.312 (3)	0.309 (2)	0.307 (3)	0.311 (3)
O2 *y*	0.0711 (3)	0.0719 (3)	0.0720 (3)	O3 *y*	0.0548 (19)	0.0618 (18)	0.061 (2)	0.063 (2)
O2 *z*	0.6845 (4)	0.6856 (4)	0,6856 (5)	O3 *z*	0.698 (4)	0.676 (2)	0.675 (2)	0.681 (3)
B_{iso}	0.89 (7)	0.86 (7)	0.77 (8)					
				O4 *x*	0.186 (5)	0.188 (2)	0.185 (3)	0.184 (3)
				O4 *y*	−0.073 (3)	−0.0684 (18)	−0.0644 (17)	−0.0659 (18)
				O4 *z*	0.176 (5)	0.180 (2)	0.177 (2)	0.175 (2)
				O5 *x*	−0.310 (5)	−0.313 (2)	−0.315 (2)	−0.313 (3)
				O5 *y*	0.578 (3)	0.5839 (18)	0.5882 (17)	0.5879 (17)
				O5 *z*	−0.695 (5)	−0.6943 (18)	−0.695 (2)	−0.696 (2)
				O6 *x*	0.819 (3)	0.816 (3)	0.809 (3)	0.808 (3)
				O6 *y*	0.4201 (19)	0.4257 (17)	0.4284 (18)	0.432 (2)
				O6 *z*	−0.175 (3)	−0.1932 (18)	−0.197 (2)	−0.190 (3)
				B_{iso}	0.56 (5)	0.58 (7)	0.71 (7)	0.63 (6)
R_p	1.62	1.79	2.11	R_p	1.70	1.68	1.90	1.88
R_{wp}	2.22	2.41	2.78	R_{wp}	2.31	2.16	2.44	2.46
R_B	2.98	3.21	2.95	R_B	3.01	2.83	3.97	3.88
χ^2	3.09	4.75	4.59	χ^2	3.35	3.01	3.77	3.81

[a] In the space group *Pnma*, *Z* = 4, with atoms in the following positions: Sc, 4*c* (*x*, 1/4, *z*); V, 4*b* (1/2,0,0); O1, 4*c* (*x*,1/4, *z*); O2, 8*d* (*x*, *y*, *z*). In the space group *P*-1, *Z* = 1, with atoms in the following positions: Sc1, 2*i* (*x*, *y*, *z*); Sc2, 2*i* (*x*, *y*, *z*); V1, 1*d* (1/2,0,0); V2, 1*b* (0,0,1/2); V3, 1*e* (1/2,1/2,0); V4, 1*g* (0,1/2,1/2); O1, 2*i* (*x*, *y*, *z*); O2, 2*i* (*x*, *y*, *z*); O3, 2*i* (*x*, *y*, *z*); O4, 2*i* (*x*, *y*, *z*); O5, 2*i* (*x*, *y*, *z*); O6 2*i* (*x*, *y*, *z*).

perovskite-type ScVO$_3$ at ambient pressure has been followed using in-situ powder X-ray diffraction. A flow of 1:3 CO:He is used to prevent oxidation of the sample. Figure 2C shows contour plots of the XRD data from room temperature to 1000 °C for the 2θ range 31−38°. It can be observed that upon heating the diffraction maxima corresponding to the perovskite cell continuously shift to lower angles due to thermal expansion. The peak intensities start to decrease at about 800 °C and disappear completely at about 900 °C. As the perovskite peaks disappear diffraction peaks corresponding to the bixbyite phase emerge at 800 °C, and consequently, both phases coexist in the temperature range 800−900 °C. This is indicative that the phase transition is first order. Therefore, we conclude that at ambient pressure and temperatures above 800 °C the high-pressure

Table 2. Selected Bond Distances and Calculated Angles As Obtained from the Refinement

	Pnma				*P*-1			
$ScVO_3$	296 K	150 K	120 K		90 K	60 K	30 K	2 K
				d (Å)				
2 × V−O1	2.038(3)	2.0359(13)	2.0355(13)	2 × V1−O1	1.971	2.0373	2.012	2.001
				2 × V2−O2	2.04	2.068	2.067	2.061
				2 × V3−O1	2.074	2.061	2.064	2.080
				2 × V4−O2	2.05	2.032	2.030	2.023
2 × V−O2	1.967(2)	1.960(2)	1.960(3)	2 × V1−O3	1.882	1.987	1.997	1.968
				2 × V1−O4	1.99	1.987	1.986	1.988
				2 × V2−O3	2.002	1.945	1.934	1.966
				2 × V2−O4	2.00	1.979	1.975	1.983
2 × V−O2	2.004(3)	2.009(3)	2.010(3)	2 × V3−O5	1.95	1.945	1.947	1.948
				2 × V3−O6	2.026	2.049	2.016	1.992
				2 × V4−O5	2.03	2.052	2.074	2.067
				2 × V4−O6	2.007	1.929	1.930	1.951
⟨V−O⟩	2.003	2.0016333	2.0018333	⟨V−O⟩	1.947	2.0037	1.998	1.986
				⟨V2−O⟩	2.014	1.997	1.992	2.003
				⟨V3−O⟩	2.017	2.018	2.009	2.007
				⟨V4−O⟩	2.029	2.004	2.011	2.0137
				angles (deg)				
V−O1−V	133.7 (4)	133.78(5)	133.80(5)	V1−O1−V3	135.6	134.7	133.7	133.4
				V2−O2−V4	132.6	132.1	132.3	133.2
V−O2−V	137.9 (3)	137.7(1)	137.66(12)	V1−O3−V2	144.6	139.8	140.0	139.8
				V1−O4−V2	136.1	138.4	138.6	137.8
				V3−O5−V4	137.3	135.0	133.4	133.9
				V3−O6−V4	133.1	137.4	139.7	140.0
α = ⟨V−O−V⟩	136.5	136.4	136.4	α = ⟨V−O−V⟩	136.6	136.2	136.3	136.4
$\omega = (180 - \alpha)/2$	21.75	21.8	21.8	$\omega = (180 - \alpha)/2$	21.7	21.9	21.8	21.8
$s = 2(a - c)/(a + c)$	0.062	0.064	0.065					
Δ[a]	0.000419	0.000493	0.000491	Δ V1	0.00117	0.00028	5.7×10^{-5}	9.3×10^{-5}
				Δ V2	0.00017	0.001357	0.00156	0.00085
				Δ V3	0.00128	0.00133	0.00114	0.00149
				Δ V4	0.00015	0.00145	0.00179	0.00112

[a] Octahedral distortion parameter $\Delta = 1/6\Sigma[(d - \langle d\rangle)/\langle d\rangle]^2$ (ref 47).

perovskite phase reverts back to the ambient pressure stable bixbyite-type structure.

3.1.4. Low-Temperature Crystallographic Transition and Magnetic Structure: Neutron Diffraction Study. Neutron data collected from room temperature down to 90 K could be fitted to the same space group *Pnma*, consistent with the powder X-ray and electron diffraction data. The evolution of lattice parameters as a function of temperature is plotted in Figure 4. It can be seen that there is little temperature dependence for the unit cell parameters, and very small variations for the V−O distances or V−O−V angles are observed. A schematic representation of one-half a unit cell of the much distorted perovskite structure of $ScVO_3$ at room temperature appears in Figure 4.

Below 90 K, the (022) reflection, among others, splits into (022) and (0−22) (Figure 5A) and a triclinic space group, *P*-1 is needed to account for the corresponding pattern. This results in four vanadium sites at low temperature (Figure 5B), which can have implications on the final magnetic structure. Below 60 K additional reflections appear in the neutron diffractograms (collected at longer wavelengths) due to magnetic long-range ordering of the V^{3+} moments. As expected for magnetic ordering, the intensities of the magnetic reflections increase as the sample is cooled further. At 2 K the magnetic reflections can be indexed on the crystallographic cell with a magnetic propagation vector $\boldsymbol{k} = (0.5, 0, 0.5)$. At 2 K, a reasonable fit, $\chi^2 = 19.7$, $R_M = 24.1$, is obtained for two noncollinear interpenetrating rock salt sublattices. All spins of both sublattices are confined to the *xz* plane, and the two sublattices form an angle of approximately 75°. Antiferromagnetic order within each sublattice is observed on the basal plane of the orthorhombic perovskite, whereas ferromagnetic ordering occurs along the unique axis, *b*. Despite the 4 vanadium atoms not being related by symmetry it was not possible to refine independently the magnetic moment of each ion due to the low intensity of the few magnetic reflections. Therefore, the present fit uses for all vanadium atoms the same magnitude of the magnetic moment, 1.8 μB at 2 K, and is considered a good first approximation to the real magnetic structure.

3.2. Transport and Magnetic Properties. *3.2.1. Magnetic Susceptibility.* The magnetic susceptibility vs temperature was

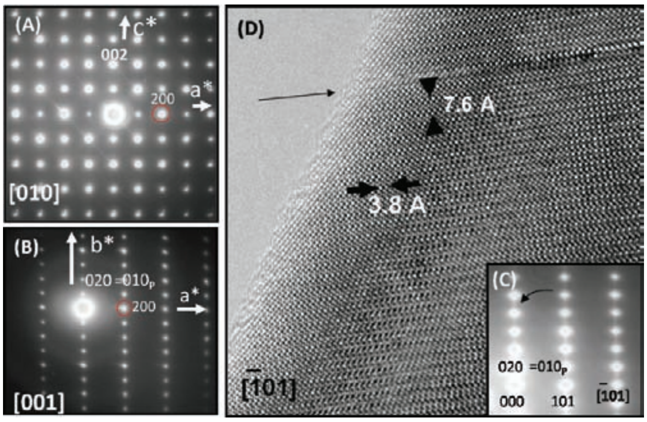

Figure 3. Electron micrographs of $ScVO_3$ pervoskite phase. Selected area electron diffraction patterns along the (A) [010], (B) [001], and (C) [−101] zone axes. (D) HRTEM image corresponding to a view along [−101].

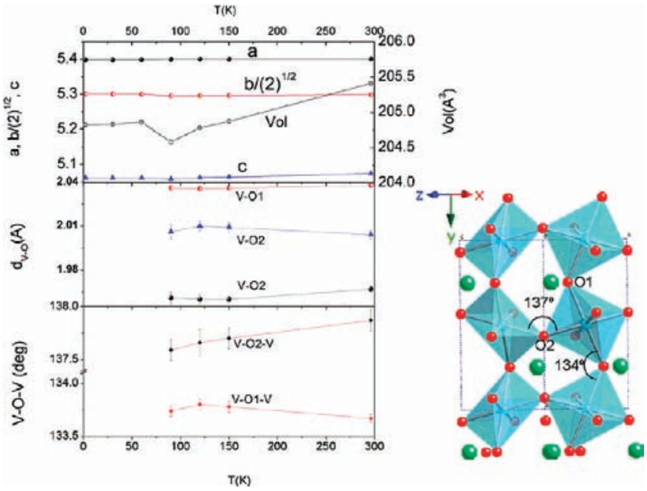

Figure 4. Crystallographic data for the $ScVO_3$ perovskite obtained from Rietveld refinements for high-resolution powder neutron diffraction patterns. (Top left) Lattice parameters defined as the square root of two of a cubic perovskite cell, a, $b/\sqrt{2}$, and c; and volume (due to angles being very close to 90° in the triclinic cell, comparison of lattice parameters is still representative). (Center left) Interatomic distances in the $[VO_6]$ octahedra. (Bottom left) V−O−V tilting angles. (Right) Schematic representation of one-half of the $ScVO_3$ unit cell at room temperature (Sc in green, V in blue, and O in red). The small V−O−V angles that largely deviate from 180° are labeled.

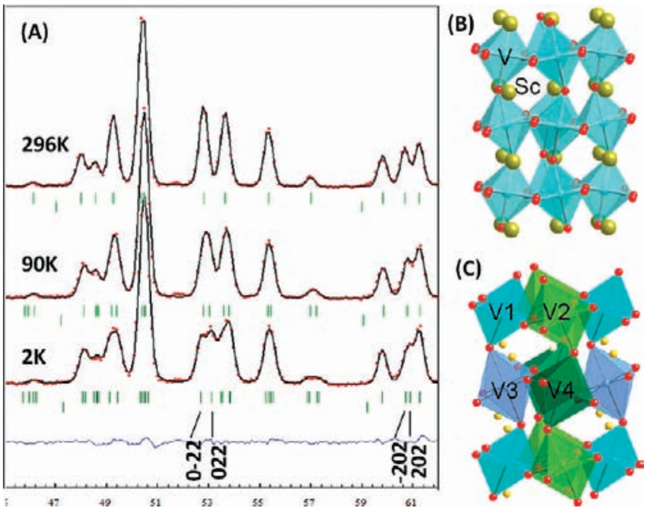

Figure 5. (A) Detail of the Rietveld refinement of the neutron diffraction profile collected at 296 (space group *Pnma*), 9K (space group *P*-1), and 2 K (space group *P*-1) with wavelength $\lambda = 1.87$ Å in the 2θ range 45−62° (B and C) Schematic representation of a unit cell of $ScVO_3$ at 296 K (B) showing the large distortion (Sc in yellow, V in blue, and O in red) and at 2 K (C) with four distinct vanadium sites (blue, light green, purple, and dark green).

measured in applied magnetic fields of 0.1 and 1 T. The inverse of the magnetic molar susceptibility data above 90 K can be fitted to the Curie−Weiss law (Figure 6A). The broad anomaly centered at about 70 K suggests the onset of magnetic short-range ordering. The derivative $d(\chi T)/dT$ shows a maximum at 57 K, which coincides with the appearance of magnetic peaks in the neutron data; thus, this maximum is the Neel temperature. The magnetic susceptibility data show ZFC-FC divergence below 30 K.

Magnetization vs applied magnetic field was measured from 0 to 9 T at 5, 32, 52, and 300 K (Figure 6B). At 32, 52, and 300 K there is no hysteresis, whereas at 5 K a small hysteresis in the low-field region is observed. The hysteresis indicates a small ferromagnetic component due to a canted antiferromagnetic ground state. At 32 K (black circles) the magnetization is lower than at 52 K (green circles), which is consistent with the susceptibility data; this trend continues up to the highest applied magnetic fields. Consequently, antiferromagnetic (AFM) ordering is kept for fields up to 9 T.

The M vs H curve for 300 K deviates from linearity for low magnetic fields; therefore, we used the susceptibility measurement at 1 T to extract the paramagnetic moment. The Curie−Weiss fit from the 1 T measurement in the temperature range 100−300 K yields $\chi^{-1} = 82.7(3) + 0.795(1)/T$, giving a Curie constant $C = 1.26$ mol/emu K. This corresponds to an effective magnetic moment $\mu = 3.17\ \mu_B$, slightly larger than the 2.82 μ_B expected for a spin-only contribution of the d^2 V^{3+} ion. The Weiss constant $\theta = -104$ K indicates strong antiferromagnetic exchange interactions.

The magnetization curve at 5 K however tends to bend for high applied magnetic fields; this indicates an increase of the ferromagnetic component due to the realignment of the vanadium spins on increasing the applied magnetic field.

3.2.2. Heat Capacity. Heat capacity measurements were performed on a sintered piece of the "as-synthesized" sample. An anomaly is clearly observed around 60 K, which is more clearly seen as a maximum in C_p/T vs T at 57 K (Figure 6C). This temperature corresponds to the magnetic ordering temperature as obtained from the maximum in $d(\chi T)/dT$ and is independently confirmed with the appearance of magnetic peaks in the neutron data. In the same C_p/T vs T plot another anomaly is seen at 89 K and is related to the structural transition identified by neutron diffraction at temperatures close to 90 K.

3.2.3. Electronic Resistance. Resistance measurements were performed on an "as-synthesized pellet" at applied magnetic fields of 0 and 9 T; the temperature dependence of the resistance is shown in Figure 6D. Below 140 K, the resistance exceeds measurable resistance of approximately 20 MΩ for the PPMS, and therefore, the signal is lost. The plot of $\ln(R(\Omega))$ vs $1/T(K)$ in that temperature range 140−300 K follows the Arrhenius law

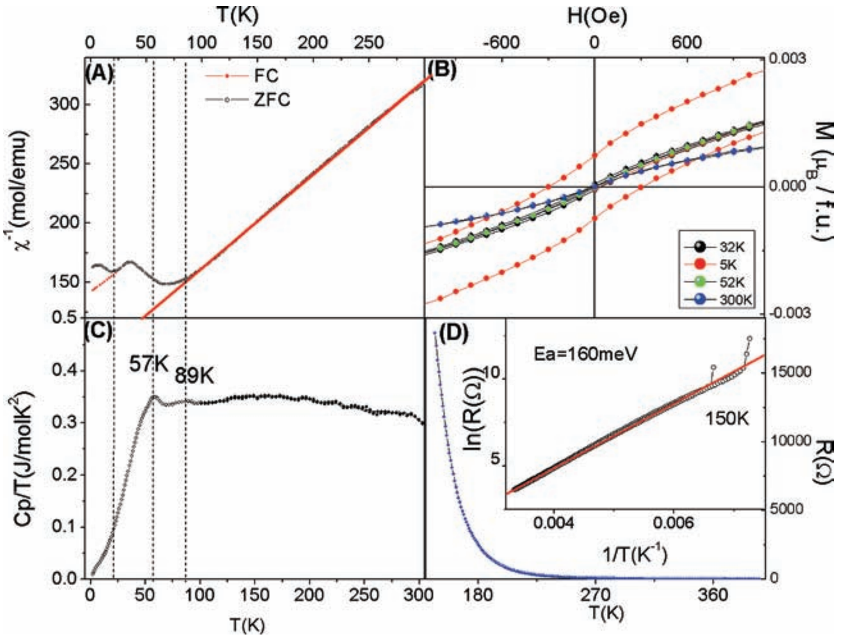

Figure 6. (A) Inverse magnetic susceptibility for the perovskite-type $ScVO_3$ versus temperature, and linear fit to the Curie–Weiss law. (B) Low-field region of the magnetization vs applied magnetic field at different temperatures. (C) C_p/T vs temperature. (D) Temperature dependence of the electrical resistance. The inset shows the logarithmic plot with the fit to an Arrhenius law at zero field and 9 T.

with a fitted activation energy of 160 meV. These findings are indicative of semiconducting behavior. No magnetic field dependence of the resistance (i.e., magnetoresistance) was observed, which is consistent with the lack of magnetic ordering at temperatures above 140 K.

4. DISCUSSION

The first point of this discussion focuses on the order–disorder phase transition and the stability of the resulting perovskite. The above results demonstrate the complete transformation from the cation-disordered bixbyite $ScVO_3$ into a fully ordered orthorhombic perovskite at high pressure. As previously shown,[18–20] high pressure can cause transitions for $(AA')_2O_3$ oxides through the path: bixbyite → corundum → Rh_2O_3 (II) → $GdFeO_3$ (*o*-perovskite) → $CaIrO_3$ (postperovskite). The bixbyite-type $ScVO_3$ shows no quenchable transformation at pressures up to 4 GPa and temperatures up to 1000 °C (Figure 2A). Increasing the pressure to 6 GPa and the temperature to 1000 °C results in a partial conversion to the cation-ordered perovskite phase, and only at 8 GPa and 800 °C complete phase conversion is observed. No structure types besides the bixbyite and perovskite are present in the quenched samples. This confirms the path of transitions of Figure 1a as a route toward the synthesis of metastable perovskites and should be generally applicable for zircon phases $AA'O_4$ that can be reduced to a bixbyite or other intermediate structure types.

On the basis of the Rietveld refinement of the room-temperature X-ray diffraction data the $ScVO_3$ perovskite crystallizes in space group *Pnma* (no. 62) with lattice parameters a = 5.4006(2) Å, b = 7.5011(2) Å, and c = 5.0706(1) Å, indicating a density increase vs the original bixbyite by 7.8%. The room-temperature lattice parameters for the $ScVO_3$ perovskite phase are in excellent agreement with the extrapolated value for the x = 1 value from the $Lu_{1-x}Sc_xVO_3$ perovskite solid solution up to x = 0.5[25] and is consistent with the decreasing size of the R cation (${}^{VIII}r_{Sc3+}$ = 0.87 Å, ${}^{VIII}r_{Lu3+}$ = 0.977 Å).[43] A perovskite with such a small R cation Sc^{3+} has a largely reduced tolerance factor, t_{ScVO3} = 0.8353 vs t_{LuVO3} = 0.8784, as calculated with SPUDs,[44] and shows a substantial increase in octahedral tilting. $ScVO_3$ thus represents a case where the tolerance factor is too small to obtain a perovskite through synthesis at ambient pressure, but it is within the limit of quencheability of the high-pressure obtained perovskites.[13]

In the new perovskite $ScVO_3$ all Sc^{3+} occupy the cuboctahedral positions, and all V^{3+} occupy the octahedral positions. Due to the slight difference in atomic number between V^{3+} and Sc^{3+}, the X-ray scattering factors are very similar; thus, the cationic ordering cannot be determined by powder X-ray diffraction. In contrast, the powder neutron diffraction data (with very different neutron scattering lengths for V and Sc) permits one to determine the cation ordering. Exchanging Sc and V positions leads to a very poor Rietveld fit. Once quenched from high pressure, the $ScVO_3$ perovskite phase is metastable at ambient conditions and does not show any sign of decomposition at room temperature after a year. The ambient-pressure in-situ powder X-ray diffraction data shown in Figure 2C only show thermal expansion below 800 °C, as can be seen by the concerted peak shift toward lower diffraction angles. At 800 °C ion mobility becomes sufficient in order to relax the perovskite back into the bixbyite phase. Between 800 and 900 °C both phases coexist without the presence of any additional reflections, thus indicating that the cation order–disorder phase transition is first order. The experiments performed during the synthesis at different conditions also showed the coexistence of both phases in the pressure range between 4 and 6 GPa and temperatures of 800–1000 °C in agreement with a first-order phase transition.

In this fully ordered perovskite, how does the room-temperature crystal structure of the quenched $ScVO_3$ perovskite compare with that of other RVO_3 perovskites? Refinement of the neutron diffraction data on the perovskite $ScVO_3$ has shown that the crystallographic structure in the studied paramagnetic region

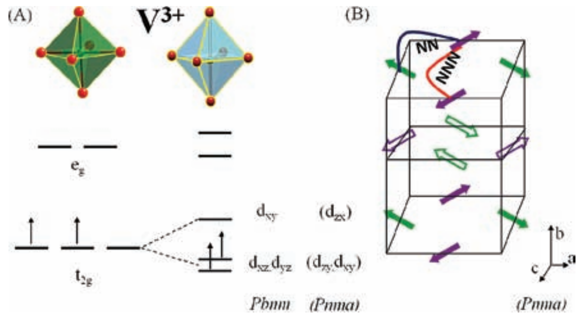

Figure 7. (A) Schematic representation of the tetragonal JT distortion for a d^2 cation in an octahedral environment. The orbital nomenclature is given for the nonstandard *Pbnm* setting frequently used in the literature for comparison (and the standard *Pnma* used here). (B) Schematic drawing of the magnetic structure of $ScVO_3$ at 2 K only showing the magnetic moments of the vanadium atoms with the two noncollinear sublattices in different colors.

(90−296 K) is orthorhombic, space group *Pnma*, as every other RVO_3 (in many instances the nonstandard setting *Pbnm* is used for simplicity). The room-temperature lattice parameters of the new synthesized $ScVO_3$ perovskite follow the sequence $c < b/\sqrt{2} < a$, which corresponds to the O-type distortion, as found in RVO_3 with small R ions, e.g., $LuVO_3$[37] and $YbVO_3$.[45] However, looking at the V−O distances a most interesting and striking result shows up since orbital ordering is already stable at room temperature.

The characteristic V−O distances in the $[VO_6]$ octahedra are listed in Table 2 and are consistent with a Jahn−Teller distortion. The V−O1 distance, defined along the $b = 2a_p$ direction, is 2.0378(11) Å, and the short and medium V−O2 distances, defined in the *ac* plane, are 1.967(2) and 2.004(3) Å. According to Figure 5A, the O-type structure and orbital ordering are observed down to 90 K. In the present $ScVO_3$ perovskite and contrary to what has been observed in all other RVO_3,[46] a cooperative Jahn−Teller-type distortion is already present at room temperature and therefore a crystallographic transition to the orbitally disordered perovskite might occur at higher temperatures as in the case of the strong JT ions Mn^{3+} (d^4) in $LaMnO_3$.[31] Analysis of V−O distances at high temperature (Figure S2, Supporting Information) as obtained from refinement of powder X-ray diffraction data has not evidenced this, but nonetheless, neutron diffraction data would be needed to unambiguously detect this.

Jahn−Teller distortions in octahedral environments are expected to occur whenever the e_g or t_{2g} orbitals are not fully occupied. However, uneven filling of doubly degenerate e_g orbitals are expected to be stabilized much more by JT distortion than uneven filling of triply degenerate t_{2g} orbitals. The JT effect for a d^2 cation in an octahedral environment is expected to be very weak and should only be observed at low temperatures. Surprisingly, in $ScVO_3$ this distortion is large even at room temperature, with an octahedral distortion parameter,[47] $\Delta_{neutron} \approx 0.0004$. This distortion is more than 6-fold larger than the next most distorted RVO_3 perovskite, $TbVO_3$ or any other orthovanadate (Table 3 of ref 46). Comparison with other orbitally ordered and disordered perovskites is detailed in Table S1, Supporting Information. The strong octahedral distortion in the $ScVO_3$ perovskite phase is intriguing as it does not follow the trend observed for RVO_3.

We wonder next what the mode of the octahedral distortion is at room temperature in a perovskite with such a low tolerance factor. Looking at the V−O distances, Table 2, it can be seen that the V−O1 distance is larger than both V−O2 distances from room temperature to 90 K, and therefore, tetragonally elongated octahedra are stabilized, but the fact that the octahedra are not perfectly tetragonal but are also distorted in the *ac* plane suggest mixing of two types of octahedral distortions, the tetragonal Q_3 and orthorhombic Q_2.

In order to compare with orbital ordering in other RVO_3 perovskites the nonstandard setting (i.e., *z* is chosen as the unique axis for the description of the t_{2g} orbitals) is being used in Figure 7. As we already mentioned the long V−O1 distance indicates the predominance of an elongated tetragonal JT distortion (Q_3) where both d_{xz} and d_{yz} orbitals lower their energy vs the d_{xy} orbital (Figure 7A) but superimposed is the Q_2 type, which alternatively lowers the energy of d_{xz} and d_{yz} with respect to each other. Therefore, the electron configuration will be the same in all vanadium atoms $d^1_{xz}d^1_{yz}$, with alternating energies for the electrons in those orbitals. It is exceptional that the $ScVO_3$ perovskite shows orbital ordering at room temperature and that the rarely found tetragonal distortion Q_3 (Γ_3^+ representation)[35] is predominant. Nevertheless, the two V−O2 distances are also very different over the whole temperature range 296−90 K, and there are still 2 possible arrangements of the Q_2 distortion mode along the *c* axis that will determine the orbital ordering between the 2 medium and 2 short V−O distances in the VO_6 octahedra.

As it has been long discussed in RVO_3 vanadates and was initially explained by Mizokawa et al. for YVO_3,[34] in perovskites with large octahedral tilting, the ubiquitous Q_2 orbital ordering arranges "in phase" along the unique axis, also named d-type Jahn−Teller distortion (that results in a C-type orbital order), vs an "out of phase" or a-type Jahn−Teller (that yields a G-type orbital order) due to an enhancement of the R−O covalent interaction produced by a shift of the R atom from its equilibrium position. Considering the room-temperature V−O−V angles, 133.7° and 137.3° as well as its evolution down to 90 K (Figure 5 and Table 2) it is noticed that this oxide perovskite shows one of the largest octahedral tiltings known to date, $\varphi_{111} = 26°$. Therefore, in $ScVO_3$ a C-type orbital order is expected to be stabilized which is in fact compatible with the observed *Pnma* symmetry, while the G-type orbital order would require a change of symmetry. Therefore, the two operational distortion modes, Q_3 and C-Q_2, are compatible with the orthorhombic symmetry *Pnma* for the most common setting of octahedral tilting (Table 2 in ref 35); still it seems unusual that it is stable at room temperature.

While recent literature indicates that all RVO_3 have initially an orbital-ordered G-type pattern (monoclinic), $ScVO_3$ shows a C-type orbital ordering. The value of $Q_2 = l_x - l_y$ and $Q_3 = (2l_z - l_x - l_y)/\sqrt{6}$ terms that describe the site distortion and the combined distortion parameter $\rho_0 = \sqrt{(Q_2^2 + Q_3^2)}$ for $ScVO_3$ at room temperature are $Q_2 = 37 \times 10^{-3}$ Å, $Q_3 = 61 \times 10^{-3}$ Å, and $\rho_0 = 71 \times 10^{-3}$ Å, much larger than the maximum $Q_2 = 31 \times 10^{-3}$ Å found in $LuVO_3$ or the maximum $Q_3 = 37 \times 10^{-3}$ Å and $\rho_0 = 40 \times 10^{-3}$ Å found in $TbVO_3$ for other RVO_3. There is a correlation between the temperature of orbital ordering and the value of the site distortion ρ_0 at room temperature, as shown in Figure 8 of ref 48. While extrapolation of T_{OO} vs ionic radii would yield a T_{OO} below room tempearature, extrapolation of T_{OO} for the value of $\rho_0 = 71 \times 10^{-3}$ Å yields temperatures for orbital ordering above room temperature.

In the spin−orbit phase diagram of Miyasaka et al.[30] an increase in the temperature of C-type orbital ordering, T_{oo2}, is observed for decreasing ionic radii of the R cations and increases indeed from 80 K in $LuVO_3$ to $T > 296$ K in $ScVO_3$. It seems however too large of a change to be solely due to the decrease of ionic radii of R and corresponding octahedral tilting. Related with this small ionic radius and small *t* is the use of high pressure, which may play a role in stabilizing the orbitally ordered phase, since during the synthesis a high-pressure phase is quenched and there is evidence that upon applying pressure the temperature of orbital ordering in RVO_3 phases increases.[48] It could be argued that the high pressure alone is not responsible for the room-temperature distortions, since $CaCrO_3$, the only other example of high-pressure synthesized orthorhombic perovskite oxide with a d^2 cation, does not show this type of orbital ordering,[49,50] but the tolerance factor of $CaCrO_3$ is not as low as for $ScVO_3$. It seems that the combination of all of these interrelated factors, high-pressure synthesis, small ionic radii, and large octahedral tilting, are responsible for the stability of the orbitally ordered phase. Since $ScVO_3$ is the most tilted RVO_3 perovskite phase we expect new physical properties that can be traced back to the extreme distortions imposed by the quenched high-pressure structure. The octahedral distortions are therefore caused by synthesis of the oxide phase, and the electronic structure is a consequence of the imposed octahedral distortions in $ScVO_3$. High-temperature powder X-ray in-situ diffraction data and DSC data do not show any evidence of a melting of the orbital ordered state. The only relaxation observed is the crystallographic transition from the cation-ordered perovskite phase to the cation-disordered bixbyite phase at approximately 900 °C.

In accordance with this predominantly $Q_3 + Q_2$ JT distortion and accompanying "C"-type orbital ordering, crystallographic and magnetic phase transitions different from those found in other RVO_3 occur at low temperatures. An anomaly is observed in heat capacity measurements at about 90 K, which corresponds to a structural transition confirmed by high-resolution neutron diffraction data collected at this temperature. Refinements for orthorhombic or monoclinic space groups yield poor agreement factors ($\chi^2 = 11$). The triclinic space group *P*-1 is needed to fit the split reflections, which at 90 K can be fit to a pseudomonoclinic cell with beta and gamma angles equal to 90° (Figure 4A) but at 60 K and below all three angles become distinct from 90°.

As for the origin of the structural transition from orthorhombic to triclinic, it does not seem to be driven by a slight increase in the orthorhombic strain, *s* in Table 2, which is 0.062 at 296 K and 0.064 at 90 K. Simultaneously, on cooling there is a very small change in the octahedral tilting and the octahedral distortion parameters remain very high. Any possible charge ordering is also ruled out since bond valence sum calculations performed with the software Bond Strasse[41] demonstrate that the vanadium valence is 3.0(1) for every vanadium atom in the whole temperature range, and this is consistent with the 2 unpaired electrons and the refined magnetic moment at 2 K being 1.8 μB; however, it is observed that the small scandium deficiency has preference for one site. On the other hand, the transition to a triclinic cell coincides with the beginning of magnetic interactions since at those temperatures the magnetic susceptibility starts deviating from the Curie–Weiss law and these could induce the structural transition; nevertheless, no long-range magnetic ordering is observed above 60 K.

Finally, below 60 K the magnetic susceptibility and neutron diffraction data show the onset of magnetic ordering of the V^{3+} sublattice magnetic moments, which is the only paramagnetic ion. In the neutron data, magnetic reflections appear at 55 K. Furthermore, a maximum in the magnetic susceptibility and specific heat data is observed at 57 K; this can be considered T_N. The new magnetic reflections cannot be refined with the $\mathbf{k} = (0, 0, 0)$ magnetic propagation vector reported for other RVO_3; however, they can be indexed on a magnetic superstructure, propagation vector $\mathbf{k} = (0.5, 0, 0.5)$, which means that the magnetic cell is $2a_p \times 2a_p \times 2a_p$. Good Rietveld fits were obtained for an antiferromagnetic alignment of the spins in two noncollinear sublattices, with the spins lying in the *xz* plane in a zigzag mode as illustrated in Figure 7. The agreement factors of the refinement have similar values for the larger component of the magnetic moment being along either the *x* or the *z* axis. This noncollinear magnetic arrangement is different from the G-type or C-type spin ordering found in other RVO_3 perovskites as expected for the different symmetry and orbital ordering observed.

The magnetic structure is determined by the path of stronger magnetic interactions, which ultimately relies on the orbital occupancies and the V–O–V distances and angles. In $ScVO_3$, V–O–V angles are significantly smaller than for any other RVO_3. Increasing both the octahedral tilting and the octahedral distortion the two vanadium 3d electrons become more localized, and therefore, the V–O–V superexchange interactions responsible for the ordering of the V^{3+} magnetic moments in the RVO_3 family become weaker, thus decreasing the Neel ordering temperatures as the R cation size decreases. Moreover, due to the very large octahedral tilting and octahedral distortion, some O–O distances become very short and next nearest neighbor (NNN) magnetic interactions through the path V–O–O–V become stronger than nearest neighbor (NN) V–O–V superexchange interactions (Figure 7B). Furthermore, because of the large distortion, anisotropic interactions with a different sign for the NNN interactions in both directions in the *xz* plane can cause the noncollinear, close to spiral antiferromagnetic arrangement.

Since the magnetic exchange path in $ScVO_3$ is different than in the other RVO_3 perovskites, a different magnetic structure is stabilized, and therefore, T_N does not continually decrease with the decreasing ionic radii in the series of rare earth cations due to the lanthanide contraction.

This type of noncollinear spin ordering resembles that observed in the multiferroelectric manganites, $Tb_{1-x}Dy_xMnO_3$, with $x = 0.59$ for which a six spin spiral magnetic structure stabilizes.[51] The fact that a similar magnetic structure is observed in a d^2 cation containing perovskite suggests the possibility of other phenomena such as ferroelectricity could occur in this compound below the crystallographic transition.

5. CONCLUSIONS

We observed the transformation of the ambient pressure $ScVO_3$, bixbyite, with statistical Sc^{3+} and V^{3+} disorder, into the fully Sc/V ordered orthorhombic perovskite (space group *Pnma*) at 80 kbar and 800 °C. The quenchable perovskite phase reverts into the disordered bixbyite structure upon heating to 900 °C in 1 bar of CO:He.

Compared to other rare earth orthovanadates, $R^{III}V^{III}O_3$, the perovskite phase $ScVO_3$ shows the smallest lattice parameters as expected for the smaller cation occupying the A position and correspondingly the largest octahedral tilting. However, this reduction in ionic radius implies also some structural aspects that have not been observed in other RVO_3 perovksites, such as the stabilization of a cooperative octahedral Jahn–Teller distortion at room temperature for this d^2 cation, as indicated by the existence of orbital ordering at room temperature and very large octahedral distortions. This orbital ordering corresponds predominantly to elongated octahedra along the unique axis, resulting in the mixing of tetragonal Q_3 and orthorhombic Q_2 distortion modes. Moreover, the perovskite distorts into a triclinic cell below 90 K with four inequivalent vanadium positions, which below 60 K order with a 1.8 μB magnetic moment in two noncollinear rock salt-type interpenetrating antiferromagnetic sublattices according to a $2a_p \times 2a_p \times 2a_p$ magnetic cell. We therefore not only extended the RVO_3 perovskite family by one member but identified a fundamental change of physical properties as a consequence of large strain, which in turn activates a new magnetic exchange path due to the large octahedral tilting. The small A-site cation therefore permits one to tune the physical properties of orthovandates and broadens the range of observed phenomena otherwise only observed in rare earth manganites, thus enhancing the concept of universality of perovskites.

■ ASSOCIATED CONTENT

Ⓢ Supporting Information. Complete list of authors of ref 49, plot of refinement of the magnetic structure at low temperature (2 K) and comparative table of orbital ordered and non orbital ordered perovskites with characteristic parameters. This material is available free of charge via the Internet at http://pubs.acs.org.

■ AUTHOR INFORMATION

Corresponding Author
ilaisza@hotmail.com; Mario_Bieringer@umanitoba.ca

Present Addresses
[‖]CIC Energigune, Parque Tecnologico, C/Albert Einstein 48, 01510, Miñano (Alava) Spain.

Notes
[⊥]Deceased.

■ ACKNOWLEDGMENT

The authors thank A. Arevalo-Lopez, A. Duran, E. Climent-Pascual, M. Leskes, and J. Carretero-Gonzalez for fruitful discussions and J. Gallardo-Amores, J. Romero de Paz, and E. Matesanz CAI-RX UCM for technical assistance. T. Hansen and the ILL is acknowledged for providing neutron beamtime and technical support. The authors thank the National Research Council-Canadian Neutron Beam Centre (NRC-CNBC) for neutron beam time support. E.C.M. thanks UCM for a contract. Funding through projects MAT2007-64004 and Comunidad Autonoma de Madrid (MATERYENER program PRICYT S-0505/PPQ-0093) is acknowledged. M.B. acknowledges NSERC and CFI for operating and infrastructure support. S.P.S. is thankful for graduate students support (UMGF) from the University of Manitoba.

■ REFERENCES

(1) Chahara, K. I.; Ohno, T.; Kasai, M.; Kozono, Y. *Appl. Phys. Lett.* **1993**, *63*, 1990–1992.

(2) Bednorz, J. G.; Müller, K. A. *Z. Phys. B: Condens. Matter* **1986**, *64*, 189–193.

(3) Huang, Y. H.; Dass, R. I.; Xing, Z. L.; Goodenough, J. B. *Science* **2006**, *312*, 254–257.

(4) Kim, C. H.; Qi, G.; Dahlberg, K.; Li, W. *Science* **2010**, *327*, 1624–1627.

(5) Oganov, A. R.; Ono, S. *Nature* **2004**, *430*, 445–448.

(6) Goldschmidt, V. M. *Naturwissenschaften* **1926**, *14*, 477–485.

(7) Glazer, A. M. *Acta Crystallogr., B* **1972**, *28*, 3384–3392.

(8) Howard, C. J.; Stokes, H. T. *Acta Crystallogr., B* **1998**, *54*, 782–789.

(9) Ali, R.; Yashima, M. *J. Solid State Chem.* **2005**, *178*, 2867–2872.

(10) Castillo-Martinez, E.; Duran, A.; Alario-Franco, M. A. *J. Solid State Chem.* **2008**, *181*, 895–904.

(11) Belik, A. A.; Yusa, H.; Hirao, N.; Ohishi, Y.; Takayama-Muromachi, E. *Chem. Mater.* **2009**, *21*, 3400–3405.

(12) Azumi, M.; Carlsson, S.; Rodgers, J.; Tucker, M. G.; Tsujimoto, M.; Ishiwata, S.; Isoda, S.; Shimakawa, Y.; Takano, M.; Attfield, J. P. *J. Am. Chem. Soc.* **2007**, *129*, 14433–14436.

(13) Hattori, T.; Matsuda, T.; Tsuchiya, T.; Nagai, T.; Yamanaka, T. *Phys. Chem. Miner,* **1999**, *26*, 212–216.

(14) Cheng, J. G.; Alonso, J. A.; Suard, E.; Zhou, J. S.; Goodenough, J. B. *J. Am. Chem. Soc.* **2009**, *131*, 7461–7469.

(15) Ruiz-Bustos, R.; Saez-Puche, R.; Gallardo-Amores, J. M.; Alario-Franco, M. A. *Phys., C: Supercond. Appl.* **2002**, *382*, 395–400.

(16) Lin, J. F.; Degtyareva, O.; Prewitt, C. T.; Dera, P.; Sata, N.; Gregoryanz, E.; Mao, H. K.; Hemley, R. J. *Nat. Mater.* **2004**, *3*, 389–393.

(17) Oganov, A. R.; Ono, S. *Proc. Nat. Acad. Sci.* **2005**, *102*, 10828–10831.

(18) Pasternak, M.; Rozenberg, G. K.; Machavariani, G. Y.; Naaman, O.; Taylor, R. D.; Jeanloz, R. *Phys. Rev. Lett.* **1999**, *82*, 4663–4666.

(19) Olsen, J. S.; Cousins, C. S. G.; Gerward, L.; Jhans, H.; Sheldon, B. J. *Phys. Scr.* **1991**, *43*, 327–330.

(20) Ono, S.; Ohishi, Y. *J. Phys. Chem. Solids* **2005**, *66*, 1714–1720.

(21) Alonso, J. A.; Casais, M. T.; Martínez-Lope, M. J. *Dalton Trans.* **2004**, *9*, 1294–1297.

(22) Yakel, H. L. *Acta Crystallogr.* **1955**, *8*, 394–398.

(23) Wold, A.; Ward, R. *J. Am. Chem. Soc.* **1954**, *76*, 1029–1030.

(24) Rogers, D. B.; Ferreti, A.; Ridgley, D. H.; Arnott, R. J.; Goodenough, J. B. *J. Appl. Phys.* **1966**, *37*, 1431–1432.

(25) Lundgren, R. J.; Cranswick, L. M. D.; Bieringer, M. *Chem. Mater.* **2007**, *19*, 3945–3955.

(26) Shannon, R. D. *Inorg. Chem.* **1967**, *6*, 1474.

(27) Park, J. H.; Parise, J. B. *Mater. Res. Bull.* **1997**, *32*, 1617.

(28) Ren, Y.; Palstra, T. T. M.; Khomskii, D. I.; Pellegrin, E.; Nugroho, A. A.; Menovsky, A. A.; Sawatzky, G. A. *Nature* **1998**, *396*, 441–444.

(29) Goodenough, J. B. *Annu. Rev. Mater. Sci.* **1998**, *28*, 1–27.

(30) Miyasaka, S.; Okimoto, Y.; Iwama, M.; Tokura, Y. *Phys. Rev. B* **2003**, *68*, 100406(R).

(31) Rodriguez-Carvajal, J; Hennion, M.; Moussa, F.; Moudden, A. H.; Pinsard, L.; Revcolevschi, A. *Phys Rev. B* **1998**, *57*, R3189–3192.

(32) Fauth, F.; Suard, E.; Caignaert, V. *Phys. Rev. B* **2001**, *65*, 060401.

(33) Bordet, P.; Chaillout, C.; Marezio, M.; Huang, Q.; Santoro, A.; Cheong, S. W.; Takagi, H.; Oglesby, C. S.; Batlogg, B. *J. Solid State Chem.* **1993**, *106*, 253–270.

(34) Mizokawa, T.; Khomskii, D. I.; Sawatzky, G. A. *Phys. Rev. B* **1999**, *60*, 7309–7313.

(35) Carpenter, M. A.; Howard, C. J. *Acta Crystallogr., B* **2009**, *65*, 134–146.

(36) Muñoz, A.; Alonso, J. A.; Casais, M. T.; Martíinez-Lope, M. J.; Martínez, J. L.; Fernandez-Díaz, M. T. *Phys. Rev. B* **2003**, *68*, 144429.

(37) Muñoz, A.; Alonso, J. A.; Casais, M. T.; Martínez-Lope, M. J.; Martínez, J. L.; Fernandez-Díaz, M. T. *Chem. Mater.* **2004**, *16*, 1544–1550.

(38) Reid, A. F.; Sienko, M. J. *Inorg. Chem.* **1967**, *6*, 521–524.

(39) Laboratorio complutense de Altas Presiones; http://www.ucm.es/info/labcoap/Instrumentation.htm.

(40) Petricek, V.; Dusek, M.; Palatinus, L. *Jana2000. The crystallographic computing system*; Institute of Physics, Praha, Czech Republic, 2000.

(41) Rodriguez-Carvajal, J. *Physica B* **1993**, *192*, 55–69.

(42) Vegas, A.; Vallet-Regi, M; Gonzalez-Calbet, J. M.; Alario-Franco, M. A. *Acta Crystallogr., B* **1986**, *42*, 167.

(43) Shannon, R. D. *Acta Crystallogr., A* **1976**, *32*, 751–767.

(44) Lufaso, M. W.; Woodward, P. M. *Acta Crystallogr., B* **2001**, *57*, 725–738.

(45) Muñoz, A.; Alonso, J. A.; Casais, M. T.; Martínez- Lope, M. J.; Martínez, J. L.; Fernandez-Díaz, M. T. *J. Mater. Chem.* **2003**, *13*, 1234–1240.

(46) Martínez-Lope, M. J.; Alonso, J. A.; Retuerto, M.; Fernandez-Díaz, M. T. *Inorg. Chem.* **2008**, *47*, 2634–2640.

(47) Alonso, J. A.; Martínez-Lope, M. J.; Casais, M. T.; Fernández-Díaz, M. T. *Inorg. Chem.* **2000**, *39*, 917–923.

(48) Zhou, J. S.; Goodenough, J. B.; Yan, J. Q.; Cheng, J. G.; Matsubayashi, K.; Uwatoko, Y.; Ren, Y. *Phys. Rev. B* **2009**, *80*, 224422.

(49) Komarek, A. C; *Phys. Rev. Lett.* **2008**, *101*, 167204.

(50) Alario-Franco, M. Á.; Castillo-Martínez, E.; Arévalo-López, A. M. *High Press. Res.* **2009**, *29*, 254–260.

(51) Arima, T.; Tokunaga, A.; Goto, T.; Kimura, H.; Noda, Y.; Tokura, Y. *Phys. Rev. Lett.* **2006**, *96*, 097202.